

Feature Profile Evolution in Plasma Processing using On-wafer Monitoring System

S. Samukawa (Professor), H. Ohtake (Associate Professor), and T. Kubota (Associate Professor)

Etching profile prediction system was developed by combination of an on-wafer sensor and simulation. We have developed on-wafer UV sensor, on-wafer charge-up sensor, and on-wafer sheath shape sensor. These sensors can measure plasma process conditions on the sample stage such as UV irradiation, charge-up voltage in high aspect ratio structures, and ion sheath condition at the plasma/surface interface. Then the output of the sensors can be used for computer simulation. The system can predict etching profile anomaly around large scale 3D structure which causes distortion of ion sheath and ion trajectory. Also, it can predict etching profile anomaly caused by the charge accumulation in high-aspect ratio holes. Also, distribution of UV-radiation damage in materials can be predicted.

5.1. Introduction

5.1.A. Background

Our life has changed since the invention of integrated circuits (ICs), which are today incorporated in every major system from automobiles to washing machines and become a basis of Information Technology. The IC industry has been expanded by shrinking the feature size of devices in ICs, since the miniaturization of devices improves the performance of devices and enables an IC chip to contain a larger amount of transistors. By following the Moore's law, which state that the number of transistors on an IC chip would be doubled every 1.4 years, the feature size of devices has been shrinking and today move in to the nanoscale regime.

ICs are fabricated on a silicon wafer by repeating film deposition, lithography, and etching. Plasma is widely used for film deposition and etching. In particular, plasma etching process contributes to the miniaturization of devices by transferring exact pattern size to underlayers. As the development of the IC manufacturing, plasma etching has been also developed to achieve high etch rate, selectivity, uniformity, and critical dimension (CD) control, and no radiation damage. However, plasma etching for the nanoscale devices today become challenging. The next-generation nanoscale devices required atomic scale control of pattern size after etching. Moreover, in these nanoscale devices, new innovative technologies are introduced such as high-k dielectric, Cu/low-k interconnects, and novel device structure (FinFETs), which make it more challenging to develop plasma etching today. Recently, these process technologies are used to fabricate microelectromechanical systems and nanoelectromechanical systems (MEMS/NEMS). To realize these devices, it is required to realize fabrication of high aspect ratio structures and three-dimensional structures. It is a new challenge for plasma processes.

5.1.B. On-wafer monitoring technique

To realize nanometer-order etching processes, process monitoring on wafer position is needed. We proposed a concept of "on-wafer monitoring", which measures kinds and energy of active species such as ions, neutrals, radicals, and photons. Conventional monitoring techniques such as Langmuir probe, quadrupole mass spectrometry, laser spectrometry, and visible/UV spectrometry have various problems such as (1) necessity of large equipment, (2) disturbance of plasma, (3) difficulty to measure real processes, and (4) not measuring on the wafer where the process occurs. To solve these problems, we fabricated various sensors using semiconductor microfabrication techniques. We have developed on-wafer UV sensor to measure UV irradiation from plasma, on-wafer charge-up sensor to measure charge-up potential across high-aspect-ratio structures under plasma irradiation, and on-wafer sheath shape sensor to measure sheath potential and thickness. By using these sensors, active species and their spatial distribution can be easily monitored in situ. We can understand the surface reaction by the measured data. Also, prediction of process damage distribution and feature profile evolution can be realized by combination of the on-wafer monitoring and computer simulation.

5.2. On-wafer UV sensor and prediction of UV irradiation damage

5.2.A. Introduction

Plasma processes are indispensable for the fabrication of ultra-large-scale-integrated circuits. In plasma, there are many activated species, such as charged particles, radicals, and photons. Using these activated species, etching and deposition processes can be realized. To precisely control plasma etching processes, it is important to understand the interaction between plasma and surfaces. In particular, the interaction of photons with a surface is not clearly understood because of the difficulty in monitoring photons during plasma processing. Several studies have reported the effects of photons on surfaces during plasma processing. High energy photons, such as ultraviolet (UV) and vacuum ultraviolet (VUV) photons, generate electron-hole pairs in SiO_2 films, resulting in various types of process damage, such as a shift in the threshold voltage of metal oxide semiconductor transistors¹ and the formation of crystalline defects.^{2,3} Additionally, since these photons can dissociate chemical bonds in sensitive materials, such as low-k dielectric films, ArF photoresist films, and organic materials, they can modify the surfaces of materials and cause process damages in those materials during plasma processing.⁴⁻⁹ To understand the effects of photons on surfaces during plasma processing and predict surface phenomena caused by UV radiation, it is necessary to obtain a UV spectrum and its absolute intensity from plasma. For this purpose, a VUV spectrograph can be used to monitor UV radiation.^{10,11} A VUV spectrograph, however, is such a large and expensive system that it is difficult to use with plasma tools in a commercial production line. Moreover, UV spectra obtained from a spectrograph do not always correspond to the UV-radiation incident to a wafer due to different fields of view. To overcome this issue with a VUV spectrograph, we have proposed an on-wafer monitoring technique, which enables the monitoring of UV photons during plasma processing on a wafer.¹²⁻¹⁵ For this study, we developed newly designed sensors for the on-wafer monitoring technique on an 8 in. commercial production line, and, using the on-wafer monitoring sensors, we established a UV spectrum prediction system, where a UV spectrum and its absolute intensity can be obtained. Additionally, we developed this system to predict low-k dielectric damage during plasma etching.

5.2.B. Experiment

1. On-wafer monitoring technique

Our newly designed on-wafer UV sensors were used in the on-wafer monitoring technique. The structure of an on-wafer UV sensor is schematically illustrated in Fig. 1. The on-wafer UV sensors were fabricated in a commercial production line and have two embedded poly-Si electrodes in dielectric films deposited on a Si wafer. The thickness of the dielectric films on the poly-Si electrodes is 150 nm. When an on-wafer UV sensor is irradiated with UV photons with higher energy shorter wavelength than the bandgap energy of the dielectric films, the UV photons are absorbed in the dielectric films and generate electron-hole pairs. By applying dc voltage between the electrodes, a “plasma-induced current” flows due to the electrons generated by UV radiation. We evaluated the UV radiation from plasma as the plasma-induced current. Since the bandgap energy depends on dielectric films, by changing dielectric films on a sensor, we can detect different UV wavelength ranges: SiO_2 for UV photons with higher energy than 8.8 eV (shorter wavelength than 140 nm) and SiN for UV photons with higher energy than 5 eV (shorter wavelength than 250 nm). In addition, for UV photons with lower energy than 5 eV (shorter wavelength than 250 nm), we used SiN/SiO_2 films. When UV photons are incident to SiN/SiO_2 , UV photons with higher energy than 5 eV (shorter wavelength than 250 nm) can be absorbed in SiN layer, resulting in the generation of electron-hole pairs. Since the bandgap energy of SiO_2 is higher than that of SiN , electrons cannot flow in the SiO_2 layer. This means that those UV photons with higher energy than 5 eV (shorter wavelength than 250 nm) do not contribute to a plasma-induced current. On the other hand, other UV photons with lower energy than 5 eV (longer wavelength than 250 nm) can penetrate through SiN/SiO_2 layers and be absorbed in the interface between SiO_2 and Si because the energy to generate electron-hole pairs at the interface between SiO_2 and Si is 3.1 eV, which is corresponding to 400 nm.¹⁶ Hence, the on-wafer UV sensor with SiN/SiO_2 can detect UV

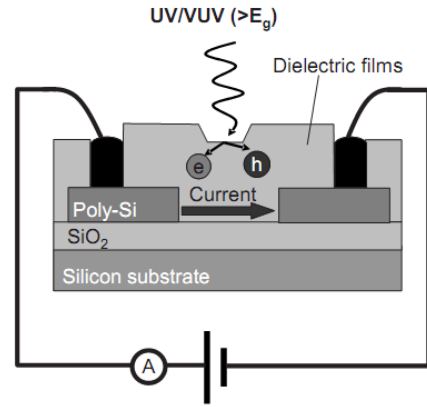


Figure 1 Structure of newly designed on-wafer UV sensor. On-wafer UV sensor has two embedded poly-Si electrodes in dielectric films deposited on Si wafer. Thickness of dielectric films on poly-Si electrodes is 150 nm.

photons with longer wavelength than 250 nm. With these three different dielectric films, a wide range of UV wavelength can be covered.

Figure 2 shows a schematic illustration of the measurement setup for the on-wafer monitoring technique with a plasma chamber. Inductively coupled plasma (ICP) (13.56 MHz) was used to generate high-density plasma of more than 10^{11} cm^{-3} . The on-wafer UV sensors were located on a stage in a plasma chamber where a wafer is usually placed and irradiated with plasma. Lead wires were attached to the electrode pads and connected to an ampere meter and a dc voltage source outside the plasma chamber. 20 V was applied to allow the plasma-induced currents to flow between the electrodes. Radio frequency (rf) filters were also used to eliminate rf signals from the plasma during measurement. In addition, a VUV spectrograph was installed at the bottom of the chamber through an 80 mm high and 1 mm diameter pinhole to measure the UV spectrum, and photons were detected at a photomultiplier tube. In the newly designed on-wafer UV sensors, electrodes were laterally arranged, which was different from previously designed on-wafer UV sensors.¹²⁻¹⁵ The previous on-wafer UV sensor measured plasma-induced currents between the surface of the sensor and an embedded poly-Si electrode through dielectric films; therefore, currents depended on the bias power applied to a wafer (Fig. 3(a)). On the other hand, in the newly designed on-wafer UV sensors, currents are measured between electrodes and do not depend on bias power (Fig. 3(b)). Therefore, our newly designed on-wafer UV sensor can be used even for etching processes with bias power.

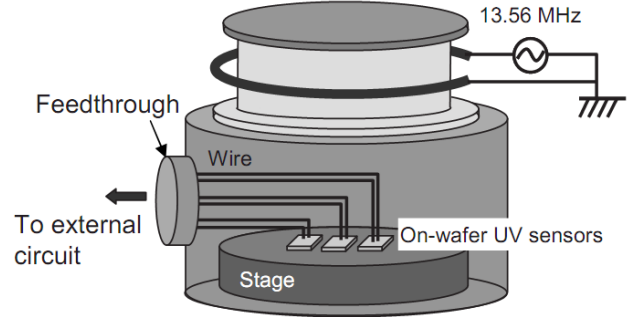


Figure 2 Schematic illustration of measurement setup for on-wafer monitoring technique with plasma chamber. On-wafer UV sensors are located on stage in plasma chamber where wafer is usually placed on and irradiated with plasma.

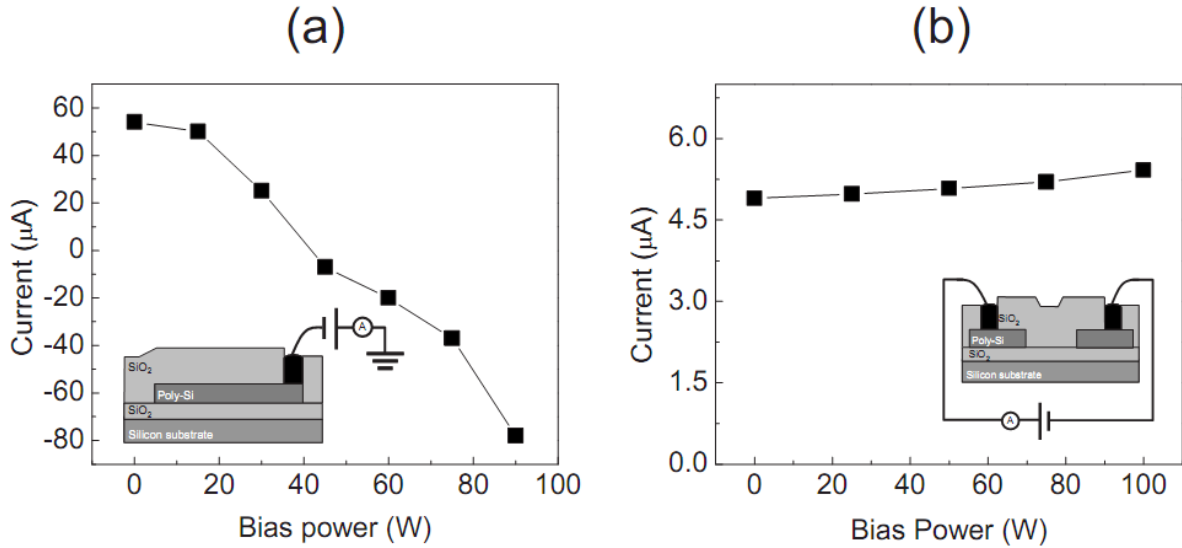


Figure 3 Bias-power dependences of plasma-induced currents in (a) previously designed on-wafer UV sensor and (b) newly designed on-wafer UV sensor.

2. Prediction system for UV spectrum

Figure 4 shows the prediction system for a UV spectrum. We used a neural network modeling technique to relate plasma-induced currents to UV spectra to develop the prediction system. The neural network modeling used in this system is shown in Fig. 5. Since it is mathematically proven that a three-layered

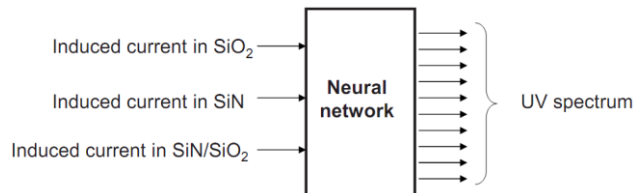


Figure 4 Prediction system for UV spectrum.

feed-forward neural network can approximate any functions, the network had a three-layered 3-5-35 neuron model. When plasma-induced currents obtained from three different on-wafer UV sensors were inputted, total intensities at intervals of 10 nm in wavelength were outputted. The network was trained on several data sets of plasma-induced currents and UV intensities measured by the VUV spectrograph. Moreover, absolute intensities of UV spectra were obtained by calibrating arbitrary units of UV intensity using a 126 nm excimer lamp.

3. Prediction system for UV-radiation damage in dielectric films

We improved the prediction system using the on-wafer monitoring technique to simulate UV-radiation damage in dielectric films during plasma etching processing. Figure 6 shows the prediction flow for UV-radiation damage in dielectric films using this technique. The on-wafer monitoring technique can provide a UV spectrum and its absolute intensity. Furthermore, UV photon trajectories directed to dielectric films were modeled by ray tracing, considering etching structures, etching rates, and etching time. In this calculation, we assumed that UV photons are radiated from the edge of ion sheaths. Based on the UV intensities incident to dielectric films, UV intensities absorbed in dielectric films are calculated with the absorption coefficient of dielectric films. By defining the rate of defect or damage generation, UV-radiation damage in dielectric films during plasma etching can be modeled. We simulated etching damage in low-k dielectric films induced by UV radiation, based on the above-mentioned damage prediction system using the on-wafer monitoring technique. In low-k dielectric films, such as SiOC films, methyl groups are incorporated to reduce the dielectric constant (k). However, SiOC films are vulnerable to plasma radiations, such as UV photons, radicals, and ions, so SiOC films are seriously damaged during plasma etching, particularly, on sidewalls of etching structures. These radiations extract methyl groups from SiOC films, resulting in an increase in the dielectric constant of SiOC films. We clarified the damage mechanism of SiCO low-k films during plasma etching⁵ and found that UV radiation plays an important role in the mechanism, namely, UV breaks Si-C bonds in SiOC films and enhances chemical reactions of SiOC films with radicals and/or moisture. To prevent SiOC films from being damaged during plasma etching and optimize etching conditions, it is important to predict damage in SiOC films during plasma etching processes. In the prediction, we defined UV-induced damage in SiOC films as the breaking of Si-O and Si-C bonds since SiOC films consist of Si-O and Si-C bonds and UV photons have enough energy to break these bonds depending on the energy/wavelength of UV photons. Chemical bonds are assumed to be broken when UV photons with higher energy (shorter wavelength) than the dissociation energy of bonds: 8.0 eV (150 nm) in Si-O bonds and 4.5 eV (275 nm) in Si-C bonds. The absorption coefficients of these bonds was supposed to be 10^6 cm^{-1} because the absorption coefficients SiO₂ and SiC dielectric films are almost same at the value of 10^6 cm^{-1} .^{17,18} According to the absorption coefficients of SiO₂ and SiC dielectric films, we assumed that Si-O and

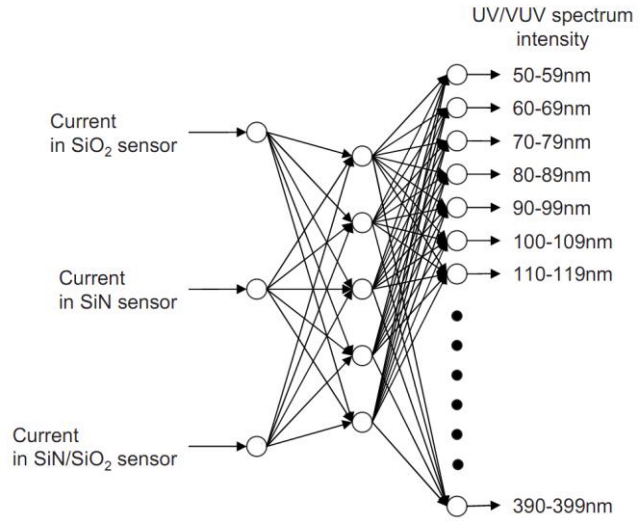


Figure 5 Neural network modeling used in prediction system for UV spectrum. Neural network had three-layered 3-5-35 neuron model. When plasma-induced currents obtained from three different on-wafer UV sensors were inputted, total intensities at intervals of 10 nm in wavelength were outputted.

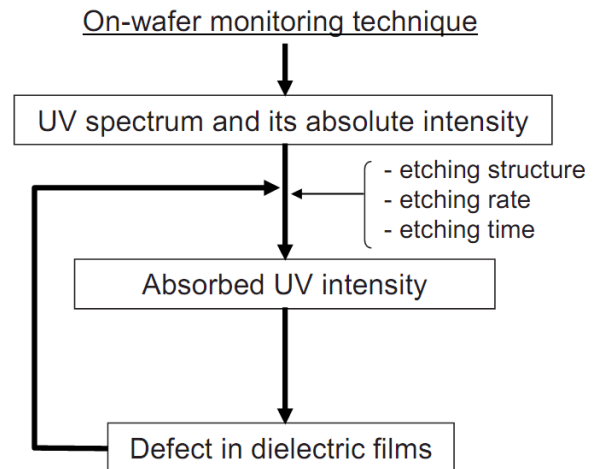


Figure 6 Prediction flow for UV-radiation damage in dielectric films using on-wafer monitoring technique..

Si-C bonds were broken by UV photons at the same rate if UV photons were above these bond dissociation energies.

5.2.C. Results and discussion

1. UV spectrum and its absolute intensity in plasma

To train the neural network used to establish the relationship between plasma-induced currents and UV spectra, we collected data sets of UV spectra and plasma-induced currents under varying conditions by changing plasma gases, ICP power, and pressure. We measured UV spectra using the VUV spectrograph and obtained arbitrary UV intensities through the measurement. The plasma-induced currents were measured using three types of on-wafer UV sensors. Figure 7 shows that the neural network prediction results for UV intensities in arbitrary units, compared to the measurement. The plotted data were not used for training the neural network. These results show that the neural network could successfully predict UV intensities. Absolute intensity of a UV spectrum was obtained by calibrating arbitrary units of UV intensity measured using the VUV spectrograph. For this calibration, we used a 126 nm excimer lamp, where the power density of UV light was approximately 5 mW/cm² at a lamp window. The lamp was installed in a chamber with the VUV spectrograph, as shown in Fig. 8. The pressure of the chamber was kept at less than 1×10^{-3} mTorr. Photon flux, Γ_λ , at a wavelength, λ , is described by the equation

$$\Gamma_\lambda = k \frac{I_\lambda}{tA}, \quad (1)$$

where k is the conversion factor, I_λ is the UV intensity (arbitrary units), t is the integrated time (0.25 s), and A is the irradiated area (0.0079 cm²). If the conversion factor can be obtained, we can calculate the photon flux of UV light from the UV intensity. Using Eq. (1), the total power density of photons, P , can be shown as the following:

$$P = \int E_\lambda \Gamma_\lambda d\lambda = \int E_\lambda \left(k \frac{I_\lambda}{tA} \right) d\lambda, \quad (2)$$

where E_λ is the energy of a photon at a wavelength of λ . On the other hand, the power density of the UV light decreased as the distance from the lamp window increased. By irradiating an on-wafer UV sensor SiO₂ with UV light from the lamp, we measured currents in the sensor, which correspond to the power density of the UV light, as a function of the distance from the lamp window, as shown in Fig. 9. From this result, we can acquire the following empirical equation of the distance dependence of the power density of the UV light:

$$P = P_0 10^{-\alpha L}, \quad (3)$$

where P_0 is the power density of the UV light at the lamp window (5mW/cm²), α is a constant (0.006), and L is the distance from the lamp window. The spectrum of the lamp measured with the VUV spectrograph is shown in Fig. 10, where a peak can be observed in the wavelength of 126 nm. By integrating UV intensities in the spectrum of the lamp and

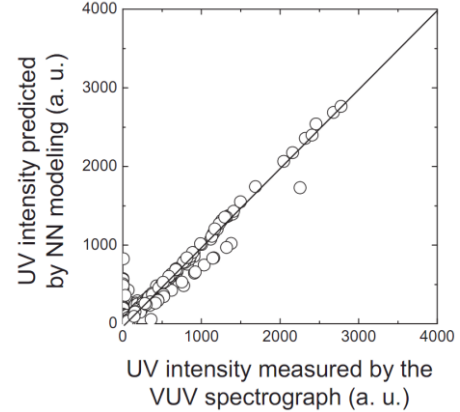


Figure 7 Comparison between UV intensities measured using VUV spectrograph and predicted with neural network.

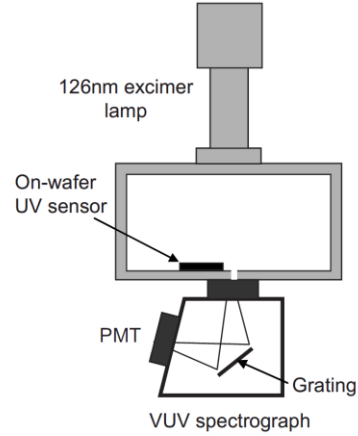


Figure 8 Schematic illustration of experimental setup for 126nm excimer lamp and VUV spectrograph.

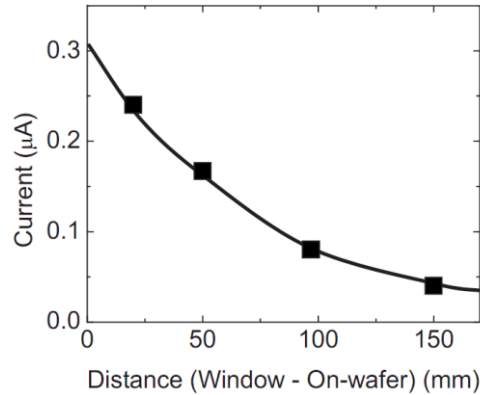


Figure 9 Currents in the on-wafer UV sensor (SiO₂) under lamp as function of distance from lamp window.

equating Eqs. (2) and (3), we obtained $k \sim 2 \times 10^9$ since the detector was located 230 mm from the lamp window. Using this conversion factor enables the calculation of absolute intensities of UV spectra.

Figure 11 shows examples of UV spectra directly measured with the VUV spectrograph (“measurement”) and obtained using the on-wafer monitoring technique and the calibration (“prediction”) in Ar, CF₃I, and C₄F₈ plasmas under the following conditions: 1000 W of ICP power, 20 SCCM (SCCM denotes cubic centimeter per minute at STP) of mass flow, and 5 mTorr of pressure. The UV spectra with the on-wafer monitoring technique agreed well with those measured with the VUV spectrograph. In addition, the comparison of the absolute intensities of UV photons between in this study and in the previous study showed a reasonable agreement. Woodworth¹¹ reported that the absolute intensity of UV photons in the wavelength range from 70 to 140 nm in C₄F₈ plasma where $n_e = 3.0 \times 10^{11} \text{ cm}^{-3}$ and $T_e = 4 \text{ eV}$ was $3.0 \times 10^{15} \text{ cm}^{-2} \text{ s}^{-1}$ based on the measurement using a VUV spectrograph. On the other hand, under the similar plasma condition (C₄F₈ plasma, $n_e \sim 3 \times 10^{11} \text{ cm}^{-3}$, and $T_e \sim 4 \text{ eV}$), the absolute intensity of UV photons in the same range was about $1 \times 10^{15} \text{ cm}^{-2} \text{ s}^{-1}$. This means that the on-wafer monitoring technique can successfully provide an UV spectrum and its absolute intensity during plasma processing.

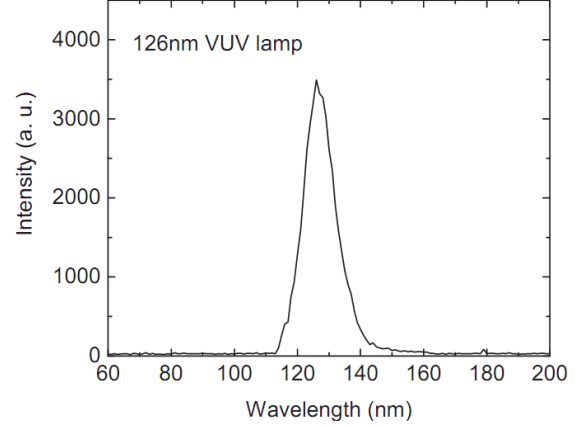


Figure 10 Spectrum of lamp measured using VUV spectrograph.

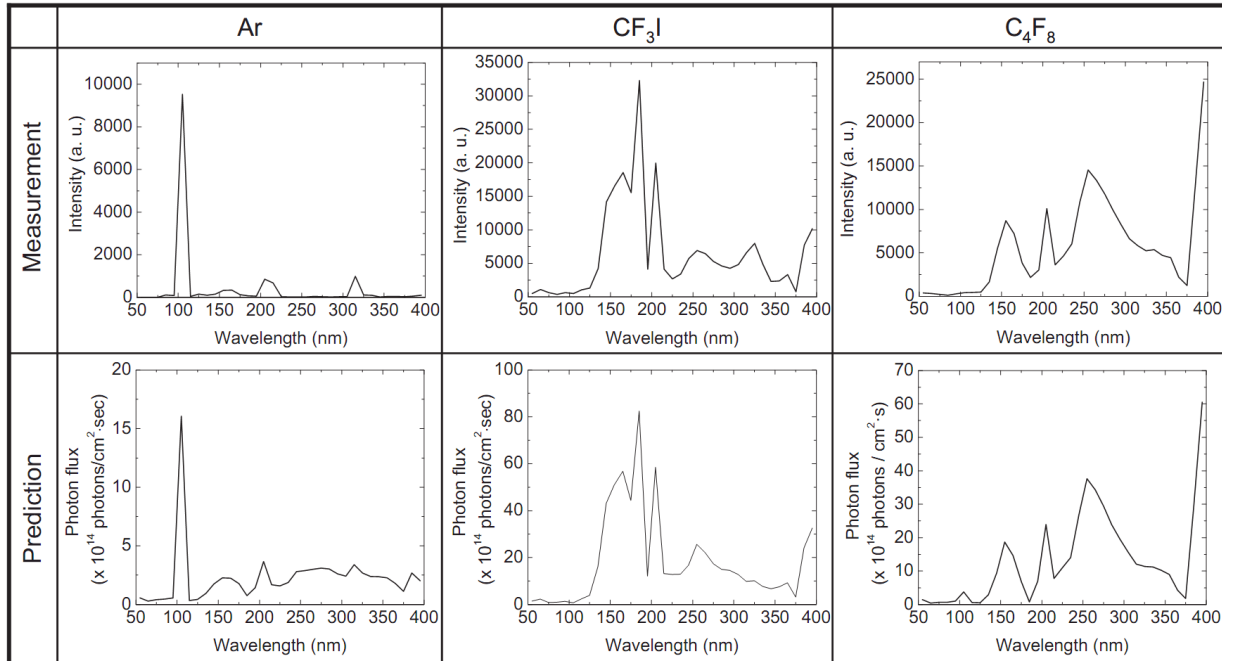


Figure 11 Examples of UV spectra directly measured using VUV spectrograph (measurement) and obtained using on-wafer monitoring technique (prediction) in Ar, CF₃I, and C₄F₈ plasmas under following conditions: ICP power of 1000 W, mass flow of 20 SCCM, and pressure of 5 mTorr.

2. UV-radiation damage in low-k dielectric films

For damage prediction, we used CF₄ plasma. The UV spectrum and its absolute intensities in CF₄ plasma were obtained using the on-wafer monitoring technique, as shown in Fig. 12. The etching structure of SiOC films with hard masks at the trench structure was modeled, as shown in Fig. 13. We assumed that the etching rate was 60 nm/min, the etching time was 100 s (just etch), and that the hard mask perfectly absorbed UV photons, namely, there was no transmission or reflection in the hard mask during plasma etching. Prediction results of damages in Si–O and

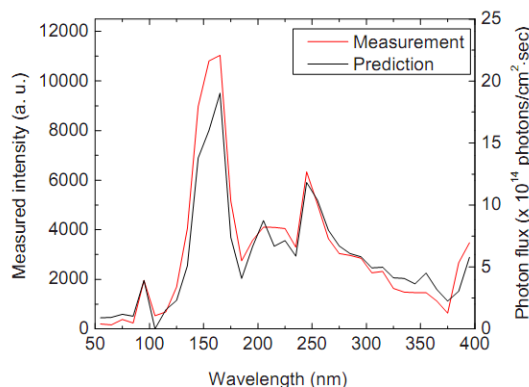


Figure 12 UV spectrum and its absolute intensities in CF₄ plasma obtained using on-wafer monitoring technique.

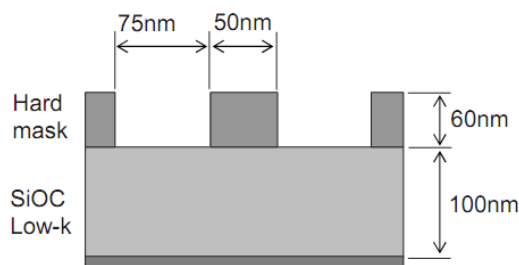


Figure 13 Model of etching structure of SiOC films with hard masks at trench. Etching rate was 60 nm/min, etching time was 100 s (just etch), and hard mask perfectly absorbed UV photons, namely, there was no transmission or reflection in hard mask during plasma etching.

Si-C bonds at 25, 50, and 100 nm of etching depths are shown in Fig. 14. These results give us several insights about UV-radiation damage in SiOC films during plasma etching. First, at the bottom of the trench structure, larger damage cannot be observed, compared to the sidewall of the trench structure. This is because the damaged layers at the bottom were removed during plasma etching. Second, the damaged layer in Si-C bonds was much larger than that in Si-O bonds. This means that during the etching of SiOC films using CF₄ plasma, most of the damage was not induced in Si-O bonds, but in Si-C bonds, because the Si-C bonds are sensitive to a wider range of UV radiation than Si-O bonds. In addition, the UV spectra in the plasmas were key in the cause of damage in SiOC films. According to the UV spectrum in CF₄ plasma, there is a smaller amount of photons in a wavelength range of less than 150 nm, compared to a range of less than 275 nm, which can also explain the difference in damage between Si-O and Si-C bonds. Finally, it was apparent that the damage layer increased as the etching progressed but damage was not found underneath the hard mask. This indicated that UV radiations were shaded by the hard mask. In other words, UV-radiation damage in SiOC films strongly depends on the geometry of the etching structure. The etching damage profile in SiOC films during CF₄ plasma was experimentally investigated by Iba.¹⁹ The etching damage profile was close to the damage layer in Si-C bonds. This means that UV photons mainly affect the side-wall surface of SiOC films during plasma etching and induce damage by breaking the bonds and enhancing chemical reactions with radicals and/or moisture. If damage is caused only by radicals, it can be observed even underneath the hard mask because radicals move isotropically and collide with other particles. It was difficult to induce damage deeply into sidewalls near the hard mask by ion bombardment because ions were accelerated by rf bias applied to the wafers. Therefore, the prediction result clarified that UV spectra and their absolute intensities are important in the damage

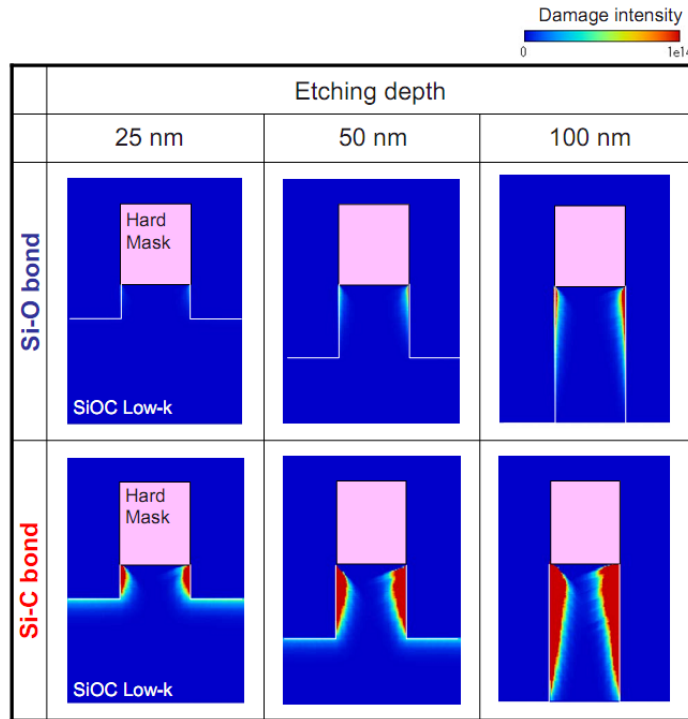


Figure 14 Prediction results of damage in Si-O and Si-C bonds at etching depths of 25, 50, and 100 nm.

formation since damage in SiOC films strongly depends on UV spectra and their absolute intensities.

5.2.D. Conclusions

UV spectra and their absolute intensities during plasma processing were predicted using our on-wafer monitoring technique. We established a neural network to relate plasma-induced currents obtained by this on-wafer monitoring technique and UV intensities measured with a VUV spectrograph. Also, we calculated the absolute intensities of UV photons by calibrating arbitrary units of the UV intensity with a 126 nm excimer lamp. UV spectra could be successfully predicted and their absolute intensities predicted using our on-wafer monitoring technique were consistent with those measured using a VUV spectrograph in a previous report. Moreover, we improved the prediction system using the on-wafer monitoring technique to simulate damages in SiOC low-k films during CF₄ plasma etching. The predicted damage profile in SiOC films was similar to the experimentally obtained damage profile. From these prediction results, we found that UV radiation damages the Si–C bonds of SiOC films during plasma etching. In addition, our results indicated that UV-radiation damage in SiOC films strongly depend on the geometry of the etching structure. The on-wafer monitoring technique should be useful in understanding the interaction of UV radiation with surface and in optimizing plasma processing by controlling the effects of UV radiation.

5.2.E. Acknowledgments

We would like to thank OKI Semiconductor Miyagi Co., Ltd. for the fabrication of on-wafer UV sensors. Also, we are grateful to Mr. Yukihiro Morimoto of Ushio Inc., Dr. Eric A. Hudson of Lam Research Corp., and Mr. Hirokazu Ueda and Dr. Toshihisa Nozawa of Tokyo Electron Technology Development Institute, Inc. for their fruitful discussions.

5.3. Prediction of Abnormal Etching Profile in High-Aspect-Ratio Via/Hole Etching Using On-Wafer Monitoring System

5.3.A. Introduction

Ultralarge-scaled Integrated circuit (ULSI) devices have many high-aspect ratio structures, such as shallow trench isolation (STI) structures, cylinder capacitors, and through-silicon vias (TSVs). These structures are fabricated by plasma etching processes. However, the generation of the abnormal profiles, such as bowing, etch stops and twisting, has been reported in high-aspect-ratio hole etching (Fig. 15). In particular, twisting is one of the severest problems in nanoscale device fabrication. Some researchers pointed out that abnormal profiles such as twisting profiles are caused by the distortion of the ion trajectory.^{20,21)} It is considered that this distortion of the ion trajectory results from the bias of charge accumulation in holes. In plasma etching, the ion sheath exists in front of the wafer owing to the energy difference between ions and electrons. Ions are accelerated into holes by the ion sheath, while electrons cannot go into holes owing to their isotropic velocity distribution. This is the so-called “electron shading effect”.²²⁾ The bottom of contact holes is positively charged, which affects the ion trajectory significantly. To avoid the ion trajectory distortion and twisting profiles, we have to observe and precisely control charge accumulation on a wafer surface. Some researchers investigated ion trajectory predictions.^{23–31)} In most of their investigations, the plasma structure and sheath area were simulated to determine potential. However, there are several problems in such predictions.

One of the severest problems is the difference between the actual and simulation values. In some simulations, the outside conditions, such as pressure, source and bias powers, and gas species, are used for the boundary conditions.^{23,24)} However, since the actual surface conditions may change for various reasons, the simulation results do not correspond to the actual ones. In other simulations, the ion/electron flux and energy were given by the authors.^{25–31)} The result in this case does not match the actual result. We have already developed and reported an on-

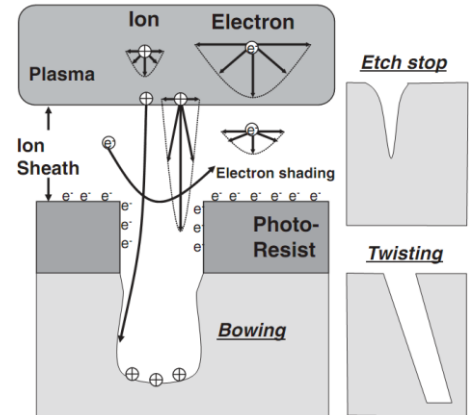


Figure 15 Bowing, etch stop and twisting in high-aspect ratio holes.

wafer monitoring technique for obtaining information on the wafer surface directly. We have shown the electron temperature, electron density, ion energy, and sidewall resistance of a hole.^{32–36)} The electron temperature and density sensor revealed a lower electron density and a higher electron temperature at the bottom of contact holes due to the electron shading effect, than in bulk plasma.³²⁾ The charge-up sensor showed that the electron shading effect could be clearly observed as the potential difference between the wafer surface and the bottom of contact holes.^{33,34)} It also revealed that a sidewall-deposited fluorocarbon film even in a high-aspect-ratio contact hole has a high electric conductivity, which may mitigate electric charge accumulation at the bottom of contact holes during SiO₂ etching processes.^{35,36)} In this study, we developed a new ion-trajectory prediction system in high-aspect-ratio holes by combining the on-wafer monitoring technique and sheath modeling to explain and predict twisting phenomena. By using the data from on-wafer monitoring sensors as the boundary conditions, the accuracy of simulation is increased. We tried to predict the potential difference between the surface and the hole-bottom in hole etching with an aspect ratio of 15 and confirmed that the simulation data corresponded to the measured data. After the simulation validity was proved, the distortion of the ion trajectory for the generation of twisting profiles was predicted.

5.3.B. Experimental and simulation models

In this study, we considered the etching of holes with a diameter of 100 nm. Figure 16 shows the simulation sequence. On-wafer sensors provided the electron temperature, electron density, surface potential, and sidewall resistance. By using these data as boundary conditions, the ion/electron motion and field potential near the wafer surface were calculated self-consistently. When the field potential is known, the ion trajectory can be calculated easily. Figure 17 shows the on-wafer sensors we used in this study. During the experiment, the on-wafer monitor was placed at the bottom of the plasma reactor. The signals were passed outside the chamber with a lead wire. The noise from the plasma was reduced using a voltage/current measurement system with an RF filter. Figure 16(a) shows our developed on-wafer probe for electron temperature and electron density.³²⁾ The on-wafer probe for electron energy is a stacked structure of Al₂O₃ (280 nm thick) and aluminum films. The Al₂O₃ film was fabricated by the anodic oxidation of aluminum. The diameter of the patterned holes was 500 nm. There were 4,800,000 holes in the monitoring device. The exposed area was 0.0942 cm². Figure 3(b) shows the charge-up sensor.³⁴⁾ Two polycrystalline silicon electrodes were separated by a 1.2-μm-thick SiO₂ film. The bottom poly-Si electrode under the SiO₂ layer was 300 nm thick. The diameter of the patterned contact holes was 100 nm and there were 150,000,000 contact holes in the monitoring device. By using the sensor, the surface and hole bottom potentials were measured directly. In addition, the sidewall resistance was also measured by measuring the resistance between the top and bottom electrodes in this sensor.

Figure 18(a) shows the simulation model using in this work, which corresponds to the structure of the charge-up sensor. We considered etching a hole with a diameter of 100 nm. In this calculation, we monitored ion and electron motions under a field potential. The governing equations are motion equations of ions and electrons, and the Poisson equation:

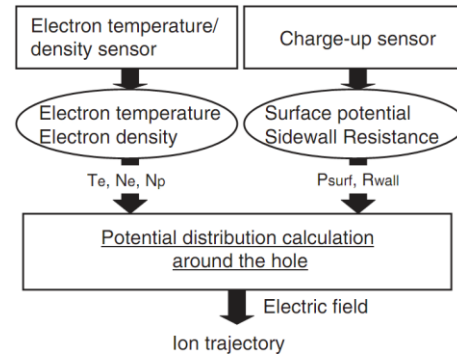


Figure 16 Concept of ion-trajectory prediction system in this study. Accurate prediction of ion trajectory can be achieved using measured values around holes by on-wafer sensors (T_e : electron temperature, N_e : electron density, N_p : plasma density, P_{surt} : surface potential, and R_{wall} : sidewall resistance).

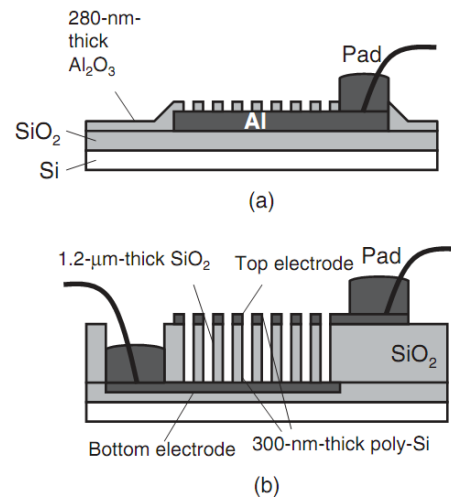


Figure 17 (a) Electron temperature/ density monitoring sensor and (b) charge-up sensor.

$$M_e \frac{d^2 r}{dt^2} = -eE, \quad (1)$$

$$M_p \frac{d^2 r}{dt^2} = eE, \quad (2)$$

$$\Delta \phi = -\frac{e(n_p - n_e)}{\epsilon_0 \epsilon_r}, \quad (3)$$

where M_e : electron mass, M_p : ion mass, r : position vector, t : time, e : elementary charge, E : electric field, ϕ : field potential, n_p : ion density, n_e : electron density, ϵ_0 : permittivity of free space, and ϵ_r : relative permittivity.

The ions and electrons were emitted 1.5 mm apart from the wafer and went to the wafer. The surface charge increased or decreased with the injection of ions or electrons, respectively. The motions of ions and electrons were affected by the field potential generated by the accumulated charge. The calculation was repeated until the field potential showed no change. According to this sequence, the ion/electron motions and field potential were solved self-consistently. The surface charge accumulation was treated in Fig. 18(b). The accumulated charge decreased with the sidewall current, followed by the sidewall resistance. Then, the equation is described as

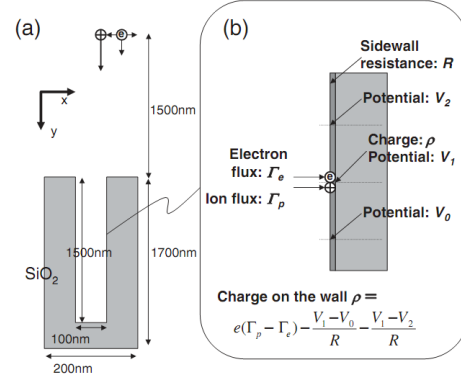


Figure 18 (a) Simulation model of this work. (b) Charge accumulation model at the sidewall of holes, considering sidewall conductivity.

$$\rho = e(\Gamma_p - \Gamma_e) - \frac{V_1 - V_0}{R} - \frac{V_1 - V_2}{R}, \quad (4)$$

here ρ : accumulated charge, Γ_p : ion flux, Γ_e : electron flux, V_1 : potential during the injection of electrons and ions, and V_0 and V_2 : potentials of adjacent cells.

5.3.C. Results and discussion

1. Ion-trajectory prediction

Figure 19 shows the calculated potential distribution around the SiO₂ hole with an aspect ratio of 15 (depth: 1.5 mm). In the simulation, the actual values measured by on-wafer sensors were used (surface potential: -42V, electron temperature: 4.3 eV, and electron density: $4 \times 10^9 \text{ cm}^{-3}$). The hole bottom was positively charged, which was due to

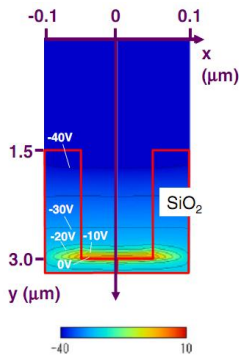


Figure 19 Calculated potential distribution around the SiO₂ hole (sidewall resistance: $3 \times 10^{15} \Omega$, surface potential: -42 V, electron temperature: 4.3 eV, and electron density: $4 \times 10^9 \text{ cm}^{-3}$).

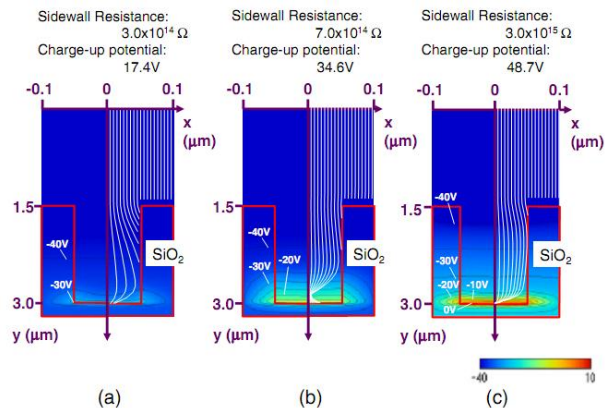


Figure 20 Calculated potential distribution and ion trajectory (white line) at sidewall resistance of (a) 3×10^{14} , (b) 7×10^{14} , and (c) $3 \times 10^{15} \Omega$ (surface potential: -42 V, electron temperature: 4.3 eV, and electron density: $4 \times 10^9 \text{ cm}^{-3}$).

the electron shading effect. Figure 20 shows the calculated potential distribution and ion trajectory as a function of sidewall resistance for observing the effect of sidewall resistance. In all cases, positive charges due to the electron shading were observed. However, the charge-up potential, which is defined as the potential difference between the surface and the hole bottom, drastically decreased with decreasing sidewall resistance. This indicates that the sidewall current reduced the positive charge at the hole bottom. In addition, the ion trajectories were distorted by the varying field potential. Thus, we have to carefully determine field potential to predict the ion trajectory precisely.

To prove the validity of the system, we compared the simulated charge-up potentials with the experimental ones. Figure 21(a) shows the calculated and measured charge-up potentials (the potential difference between the hole top and bottom) as a function of sidewall resistance. The charge-up potential drastically decreases with decreasing sidewall resistance in both cases. The simulated charge-up potential was almost the same value as the measured one. This indicates that the experimental data can be predicted using this system, proving the validity of this method. Figure 21(b) shows the mechanism of the charge reduction at a low sidewall resistance. Electrons accumulate at the surface owing to the energy difference between the electrons and ions regardless of sidewall resistance. At that time, electrons cannot go into the hole because of electron shading. At a high sidewall resistance, the charge separation is not solved because no transport of charges occurs. However, electrons can move from the wafer surface to the hole bottom at a low sidewall resistance, which causes the reduction in positive charge at the hole bottom. Accordingly, we found that sidewall resistance plays an important role in determining field potential and ion trajectory.

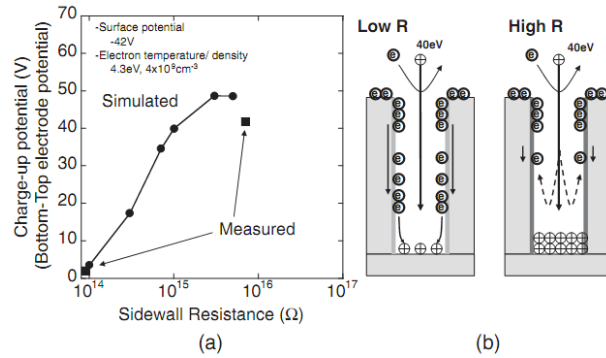


Figure 21 (a) Calculated and measured charge-up voltages as a function of sidewall resistance. (b) Mechanism of charge-up reduction by decreasing sidewall resistance.

2. Twisting prediction

Some researchers have pointed out that twisting profiles are caused by the bias of charge accumulation due to resist malformation and deposited films. ^{20,21,37-40)} However, precise mechanisms of the generation of twisting profiles remain unknown. Figure 8(a) shows an example of twisting profiles observed in our laboratory, [inductively coupled plasma (ICP) etcher, Ar : C_4F_8 = 9:1, total flux: 30 sccm, pressure: 30 mTorr, ICP power: 1 kW (13.56 MHz), bias power: 100 W (1 MHz)]. This was a dense hole pattern where the hole size and space were 100 and 100 nm, respectively. However, the actual sizes of the hole and space changed with resist deformation. From the scanning electron microscopy (SEM) image, we find that the hole profiles were distorted. We also observed that the distortion of the hole became larger as pattern space decreased. Figure 22(b) shows the relationship between pattern space and taper angle of holes in Fig. 22(a). Pattern space was defined as the pattern space on the SiO_2 surface because the resist was deformed. Taper angle was defined as the taper angle on the right side and at the bottom of the hole located on the left side of the measured space. This is because the SEM image was clear. Taper angle decreased with decreasing pattern space. Although the charge accumulation was thought to be one of reasons for the generation of twisting profiles, the effect of pattern space has not yet been discussed. Then, the ion trajectory prediction for generating twisting profiles was attempted using our developed ion trajectory prediction scheme, which can predict the charge accumulation and ion trajectory in the isolated hole [Fig. 7(a)]. The results of the on-wafer monitoring in the plasma shown in Fig. 8(a) are as follows: surface potential: -35V, electron temperature: 4.0 eV, electron density: $5 \times 10^9 \text{ cm}^{-3}$, and sidewall resistance: $3 \times 10^{15} \Omega$. Figure 23 shows the simulation model that

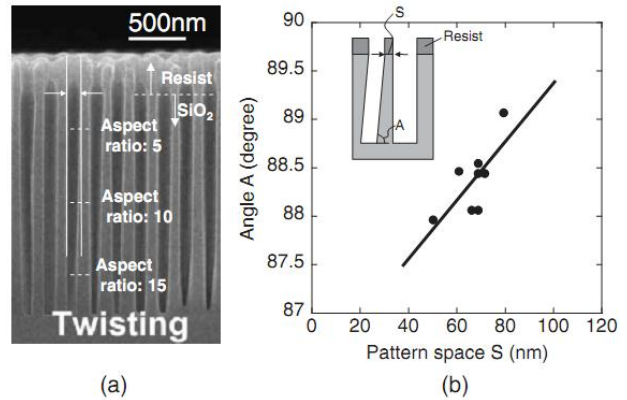


Figure 22 (a) SEM image of contact holes. (b) Dependence of taper angle on pattern space.

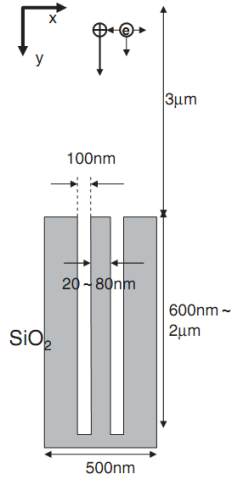


Figure 23 Simulation model for evaluating twisting profile generation.

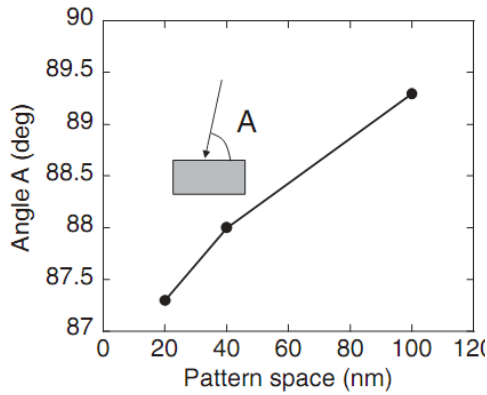


Figure 25 Incident angle of ion to the hole bottom under the conditions shown in Fig. 10.

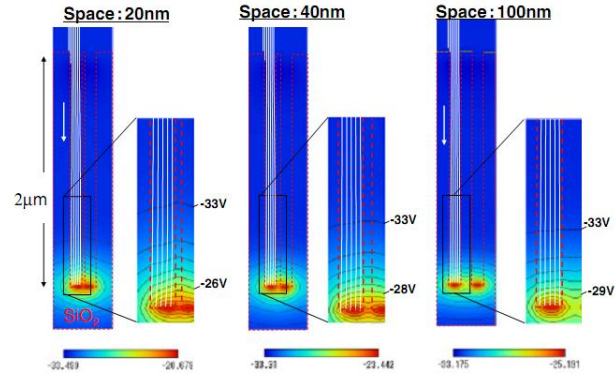


Figure 24 (a) Calculated potential distribution and ion trajectory (white line) at pattern spaces of 20, 40, and 100 nm at an aspect ratio of 20. As space decreases, the ion trajectory is distorted further (surface potential: 35 V, electron temperature: 4.0 eV, electron density: $5 \times 10^9 \text{ cm}^{-3}$, and sidewall resistance: $3 \times 10^{15} \Omega$).

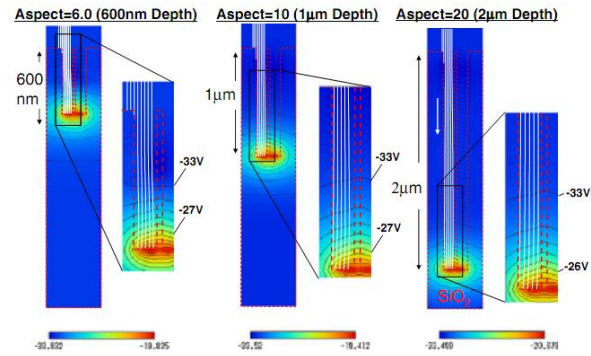


Figure 26 Calculated potential distribution and ion trajectory (white line) at aspect ratios of 6, 10, and 20 at a pattern space of 20nm (surface potential: -35 V , electron temperature: 4.0 eV, and electron density: $4 \times 10^9 \text{ cm}^{-3}$, and sidewall resistance: $3 \times 10^{15} \Omega$).

has two holes. Actually, the effect of accumulated charges of adjacent holes on the ion trajectory is very complicated because there are many holes and resist trajectory was predicted using the minimum unit, that is, in the most adjacent hole on the ion trajectory when

charges of adjacent holes on the ion trajectory is very deformation cannot be predicted. In this study, the ion two holes, to observe the effect of accumulated charges pattern space decreases due to resist deformation.

Figure 24 shows the calculated potential distribution and ion trajectory as a function of the space between the holes at an aspect ratio of 20. In the simulation, the actual values measured by on-wafer sensors were used (surface potential: -35 V , electron temperature: 4.0 eV, electron density: $5 \times 10^9 \text{ cm}^{-3}$, and sidewall resistance: $3 \times 10^{15} \Omega$). The ion trajectory at a small space was distorted more than that at a large space. At a small space (20 or 40 nm), the ions are accelerated to the opposite side of the adjacent hole. To clarify the difference between the results, the incident angle of ions as a function of pattern space is shown in Fig. 25. This figure clearly shows that the ion trajectory was distorted at a small pattern space. At a pattern space of 40 nm, the simulated taper angle was almost the same as the experimental taper angle [Fig. 22(b), about 88°].

Figure 26 shows the calculated potential distribution and ion trajectory as a function of the aspect ratio at a pattern space of 20 nm. The actual values measured by on-wafer sensors were also used (surface potential: -35 V , electron temperature: 4.0 eV, electron density: $5 \times 10^9 \text{ cm}^{-3}$, and sidewall resistance: $3 \times 10^{15} \Omega$). The ion trajectory at an aspect ratio of 6 was almost straight to the hole bottom. However, the ion trajectory was distorted at a high

aspect ratio. Figure 27 shows the summary of incident angle as a function of aspect ratio. At a higher aspect ratio, ion trajectory distortion occurs.

Figure 28 shows the mechanism of ion trajectory distortion in this study. Positive charges can be accumulated regardless of pattern space. However, the ion trajectory can be affected not only by the positive charge of the hole bottom but also by the positive charge of the adjacent hole bottom. As pattern space decreases due to resist deformation, it is possible that the positive charges that accumulated in the adjacent hole affect the ion trajectory. It should be noted that these predictions shown in Figs. 24–27 do not precisely correspond to the actual ion trajectory distortion because the ion trajectory changes with the reflection in the resist shoulder, the change in sidewall resistance, the effect of many holes, and other factors.³⁷⁾ However, it is considered that pattern space is one of reasons for the generation of twisting profiles, according to the above predictions.

5.3.D. Conclusions

An ion-trajectory prediction system for use in high-aspect-ratio hole etching was developed by combining the on-wafer monitoring technique and sheath modeling. This system revealed that sidewall conductivity strongly affects the charge-up and ion trajectory in high-aspect-ratio holes. It was also revealed that the decrease in pattern space is one of reasons for the generation of twisting profiles. This prediction system is an effective tool for developing nanoscale fabrication.

5.3.E. Acknowledgements

We would like to thank Mr. I. Kurachi, J. Hashimoto, and S. Kawada for their preparation of on-wafer sensors and for helpful discussion. We also thank Mr. T. Ozaki for his assistance with the experiments.

5.4. Feature Profile Evolution in Plasma Processing using Wireless On-wafer Monitoring System

5.4.A. Introduction

Precise plasma processes are indispensable for the fabrication of ULSI and MEMS devices. However, plasma induces damages to the devices due to irradiation of high energy ultraviolet (UV) photons^{41,42} and charged particles^{43,44}. As shown in Fig. 29, high energy UV photons from plasma chemical bonds to generate defects and degrade device performance. Charged particles cause charge-up damage and etching shape anomaly.

To solve these problems we have been developing On-Wafer Monitoring System by combination of measurement and simulation^{45,46}. A remarkable feature of this system is that the sensors to measure plasma irradiation damage are fabricated using standard microfabrication technology on silicon wafer. The measurement is performed on the sample stage position of the plasma chamber. Secondly, by combination with measurement circuit, real-time measurement can be performed. Measured data are stored in a memory in the circuit, and then, after

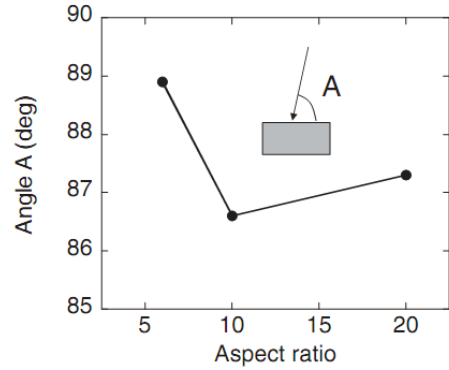


Figure 27 Incident angle of ion to the hole bottom under the conditions shown in Fig. 12.

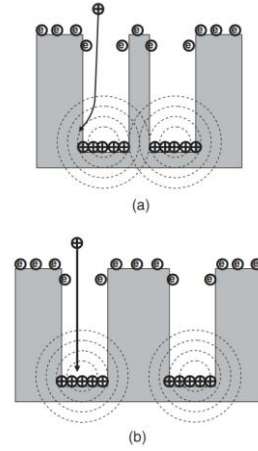


Figure 28 Mechanism of generation of twisting profiles. As pattern space decreases owing to resist deformation, positive charges that accumulated at the adjacent hole affect the ion trajectory.

unloading the sensor and the circuit, the measured data can be transferred to a PC with infra-red communication. Thirdly, prediction of damage distribution and etching profile is possible by fusion of measurement and simulation^{47,48}.

Some MEMS devices have larger scaled 3D structures comparable to the ion sheath thickness on the surface in plasma processing. In such cases, because of distortion of sheath shape due to the MEMS structure, ions trajectory are distorted to the surface and it causes etched shape anomaly as shown in Fig. 30. To solve this problem, we

developed an on-wafer monitoring system to measure ion sheath condition and predict etching shape anomaly.

5.4.B. Experimental

Prediction of etching profile anomaly can be performed by combination of sheath measurement and simulation. Etching profile is mainly ruled by ion trajectory in case of ion-assisted etching and the trajectory is determined by the sheath electric field. Therefore we developed a sensor to measure thickness and voltage of the ion sheath. Figure 31 shows the structure of the developed on-wafer sheath shape sensor. It has a numerous small electrodes to measure the surface potential and ion saturation current at wafer surface. Sheath thickness can be calculated based on the measured results.

Relationship between sheath condition and etching profile was investigated using the sensor. Etching shape anomaly was investigated by silicon etching using chlorine inductively coupled plasma. In the experiment, samples with vertical step and trench pattern was used as 3D structure sample as shown in Fig. 2. Ion sheath conditions were measured for the same plasma conditions as the etching experiment. As a result, database of relationship among ion sheath conditions, 3D step height, and etching anomaly was constructed.

Etching profile prediction system was developed based on neural network. The database was used for learning of the neural network.

5.4.C. Results and Discussion

Figure 32 shows results of on-wafer sheath shape sensor measurements. It was found that the sheath thickness and voltage were measured successfully using the newly

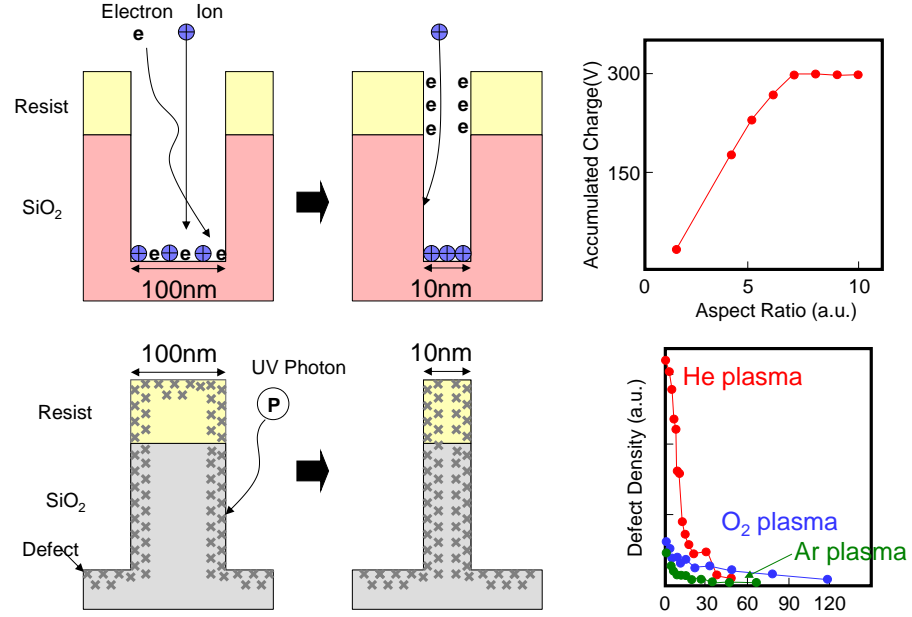


Figure 29 Schematic of plasma irradiation damage: (a) charge-up damage and (b) UV irradiation damage.

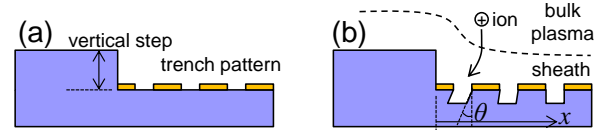


Figure 30 Schematic illustration of etching shape anomaly in 3D structure etching due to ion sheath distortion. (a) shows the structure of a 3D sample. (b) shows a schematic of the distortion of the ion sheath, ion trajectory, and etching profile due to the step.

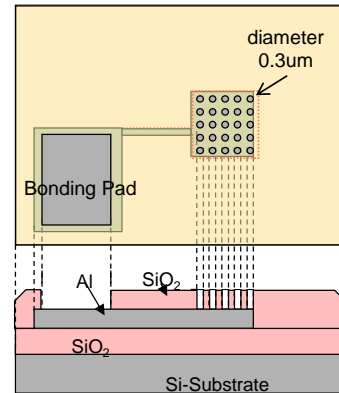


Figure 31 Structure of sheath shape sensor.

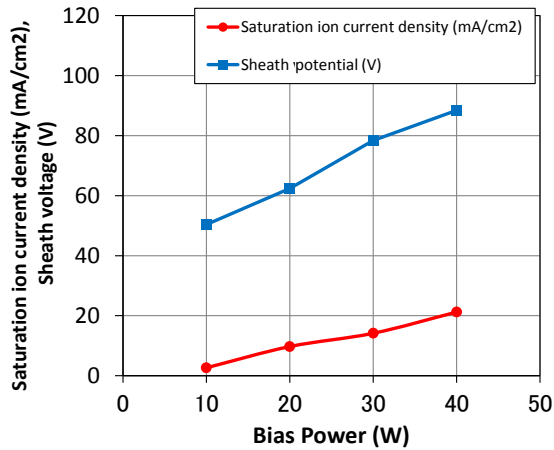


Figure 32 Results of sheath shape sensor measurements of chlorine inductively coupled plasma as a function of bias power.

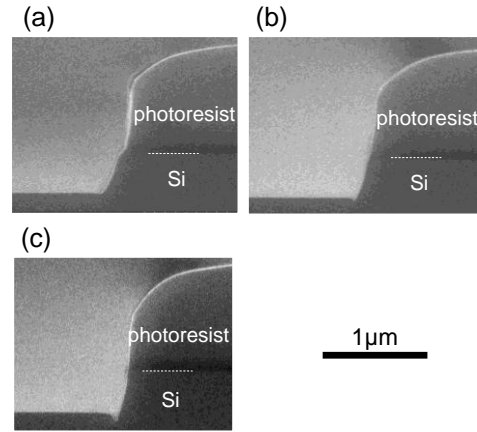


Figure 33 Cross-sectional SEM images of 3D samples after etching at distance from vertical step of (a) 200 μm , 600 μm , and 1800 μm .

developed on-wafer sheath shape sensor. Figure 33 shows SEM images of the 3D samples after chlorine plasma etching. It was found that sidewall of the etching profile was distorted and the distortion was more significant near the vertical step. The closer the distance from the step, the larger the distortion angle. This indicates that the distortion is due to the ion sheath distortion around the vertical step.

Figure 34 shows an example of etching profile prediction. It was shown that etching profile distortion around a vertical step was successfully predicted by the prediction system developed by combination of on-wafer sheath shape sensor and neural network.

5.4.D. Conclusions

Etching profile anomaly occurs around large scale 3D structure due to distortion of ion sheath and ion trajectory. A prediction system of such etching anomaly was developed by combination of on-wafer sheath shape sensor and simulation based on neural network and database. The sensor could measure the sheath voltage and thickness. The database was built by the sensor measurement and etching experiment with samples with a large vertical step. Finally the prediction system could predict the etching shape anomaly around a large vertical step.

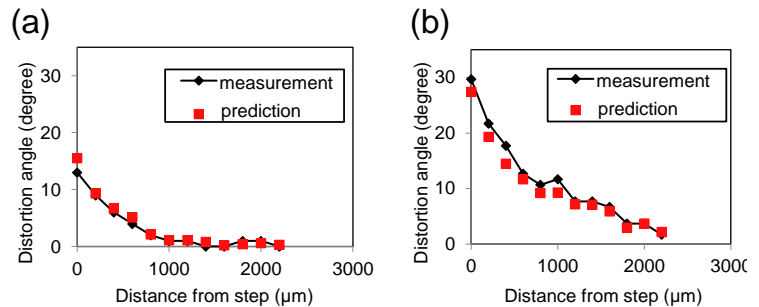


Figure 34 Measured and predicted distortion angle of etching profile of 3D sample as a function of distance from vertical step.

References

- ¹T. Yunogami, T. Mizutani, K. Suzuki, and S. Nishimatsu, Jpn. J. Appl. Phys., Part 1 **28**, 2172 (1989).
- ²T. Tatsumi, S. Fukuda, and S. Kadomura, Jpn. J. Appl. Phys., Part 1 **32**, 6114 (1993).
- ³T. Tatsumi, S. Fukuda, and S. Kadomura, Jpn. J. Appl. Phys., Part 1 **33**, 2175 (1994).
- ⁴D. Nest, D. B. Graves, S. Engelmann, R. L. Bruce, F. Weirboeck, G. S. Oehrlein, C. Andes, and E. A. Hudson, Appl. Phys. Lett. **92**, 153113 (2008).
- ⁵B. Jinnai, T. Nozawa, and S. Samukawa, J. Vac. Sci. Technol. B **26**, 1926 (2008).
- ⁶B. Jinnai, K. Koyama, K. Kato, A. Yasuda, H. Momose, and S. Samukawa, J. Appl. Phys. **105**, 053309 (2009).
- ⁷E. Soda, N. Oda, S. Ito, S. Kondo, S. Saito, and S. Samukawa, J. Vac. Sci. Technol. B **27**, 649 (2009).
- ⁸S. Uchida, S. Takashima, M. Hori, M. Fukasawa, K. Ohshima, K. Nagahata, and T. Tatsumi, J. Appl. Phys. **103**, 073303 (2008).
- ⁹S. Samukawa, Y. Ishikawa, K. Okumura, Y. Sato, K. Tohji, and T. Ishida, J. Phys. D: Appl. Phys. **41**, 024006 (2008).

- ¹⁰J. R. Woodworth, M. G. Blain, R. L. Jarecki, T. W. Hamilton, and B. P. Aragon, *J. Vac. Sci. Technol. A* **17**, 3209 (1999).
- ¹¹J. R. Woodworth, M. E. Riley, V. A. Arnatucci, T. W. Hamilton, and B. P. Aragon, *J. Vac. Sci. Technol. A* **19**, 45 (2001).
- ¹²S. Samukawa, Y. Ishikawa, S. Kumagai, and N. Okigawa, *Jpn. J. Appl. Phys., Part 2* **40**, L1346 (2001).
- ¹³M. Okigawa, Y. Ishikawa, and S. Samukawa, *J. Vac. Sci. Technol. B* **21**, 2448 (2003).
- ¹⁴Y. Ishikawa, Y. Katoh, M. Okigawa, and S. Samukawa, *J. Vac. Sci. Technol. A* **23**, 1509 (2005).
- ¹⁵M. Okigawa, Y. Ishikawa, and S. Samukawa, *J. Vac. Sci. Technol. B* **23**, 173 (2005).
- ¹⁶R. Williams, *Phys. Rev.* **140**, A569 (1965).
- ¹⁷H. R. Philipp and D. P. Edward, *Handbook of Optical Constants of Solids* (Academic, Burlington, 1997), p. 719.
- ¹⁸W. J. Choyke, E. D. Palik, and D. P. Edward, *Handbook of Optical Constants of Solids* (Academic, Burlington, 1997), p.587.
- ¹⁹Y. Iba, S. Ozaki, M. Sasaki, Y. Kobayashi, T. Kirimura, and Y. Nakata, "Mechanism of porous low-k film damage induced by plasma etching radicals," *Microelectron. Eng.* **87**, 451 (2010).
- ²⁰A. A. Ayon, S. Nagle, L. Frechette, A. Epstein, and M. A. Schmidt: *J. Vac. Sci. Technol. B* **18** (2000) 1412.
- ²¹J. Saussac, J. Margot, and M. Chaker: *J. Vac. Sci. Technol. A* **27** (2009) 130.
- ²²K. Hashimoto: *Jpn. J. Appl. Phys.* **32** (1993) 6109.
- ²³A. Sankaran and M. J. Kushner: *J. Vac. Sci. Technol. A* **22** (2004) 1242.
- ²⁴F. Hamaoka, T. Yagisawa, and T. Makabe: *J. Phys. D* **42** (2009) 075201.
- ²⁵Y. Osano, M. Mori, N. Itabashi, K. Takahashi, K. Eriguchi, and K. Ono: *Jpn. J. Appl. Phys.* **45** (2006) 8157.
- ²⁶Y. Osano and K. Ono: *J. Vac. Sci. Technol. B* **26** (2008) 1425.
- ²⁷T. G. Madziwa-Nussinov, D. Arnush, and F. F. Chen: *IEEE Trans. Plasma Sci.* **35** (2007) 1388.
- ²⁸J. Matsui, K. Maeshige, and T. Makabe: *J. Phys. D* **34** (2001) 2950.
- ²⁹J. Matsui, N. Nakano, Z. L. Petrovic, and T. Makabe: *Appl. Phys. Lett.* **78** (2001) 883.
- ³⁰K. Nishikawa, H. Ootera, S. Tomohisa, and T. Oomori: *Thin Solid Films* **374** (2000) 190.
- ³¹G. S. Hwang and K. P. Giapis: *Appl. Phys. Lett.* **71** (1997) 458.
- ³²H. Ohtake, B. Jinnai, Y. Suzuki, S. Soda, T. Shimmura, and S. Samukawa: *J. Vac. Sci. Technol. B* **25** (2007) 400.
- ³³T. Shimmura, Y. Suzuki, S. Soda, S. Samukawa, M. Koyanagi, and K. Hane: *J. Vac. Sci. Technol. A* **22** (2004) 433.
- ³⁴B. Jinnai, T. Orita, M. Konishi, J. Hashimoto, Y. Ichihashi, A. Nishitani, S. Kadomura, H. Ohtake, and S. Samukawa: *J. Vac. Sci. Technol. B* **25** (2007) 1808.
- ³⁵T. Shimmura, S. Soda, S. Samukawa, M. Koyanagi, and K. Hane: *J. Vac. Sci. Technol. B* **20** (2002) 2346.
- ³⁶T. Shimmura, S. Soda, S. Samukawa, M. Koyanagi, and K. Hane: *J. Vac. Sci. Technol. B* **22** (2004) 533.
- ³⁷M. A. Vyvoda, M. Li, D. B. Graves, H. Lee, M. V. Malyshev, F. P. Klemens, J. T. C. Lee, and V. M. Donnelly: *J. Vac. Sci. Technol. B* **18** (2000) 820.
- ³⁸S. C. Park, S. Lim, C. H. Shin, G. J. Min, C. J. Kang, H. K. Cho, and J. T. Moon: *2005 Dry Process Int. Symp.*, 2005, p. 5.
- ³⁹S. K. Lee, M. S. Lee, K. S. Shin, Y. C. Kim, J. H. Sun, T. W. Jung, D. D. Lee, G. S. Lee, S. C. Moon, and J. W. Kim: *2005 Dry Process Int. Symp.*, 2005, p. 3.
- ⁴⁰H. Mochiki, K. Yatsuda, S. Okamoto, and F. Inoue: *AVS 56th Int. Symp.*, 2009, PS2-MN-WeA-4.
- ⁴¹S. Samukawa, Y. Ishikawa, and M. Okigawa, *Jpn. J. Appl. Phys.*, **40** (2001), L1346.
- ⁴²T. Yunogami, T. Mizutani, K. Suzuki, and S. Nihimatsu, *Jpn. J. Appl. Phys.*, **28** (1989), 2172.
- ⁴³S. Murakawa, S. Fang, and J. P. McVittie, *Appl. Phys. Lett.*, **64** (1994), 1558.
- ⁴⁴K. Hashimoto, *Jpn. J. Appl. Phys.*, **33** (1994), 6013.
- ⁴⁵S. Samukawa, Y. Ishikawa, S. Kumagai, and M. Okigawa, *Jpn. J. Appl. Phys.*, **40** (2001), L1346.
- ⁴⁶T. Shimmura, Y. Suzuki, S. Soda, S. Samukawa, M. Koyanagi, and K. Hane, *J. Vac. Sci. Technol. A* **22** (2004), 433.
- ⁴⁷B. Jinnai, S. Fukuda, H. Ohtake, and S. Samukawa, *J. Appl. Phys.* **107** (2010), 043302.
- ⁴⁸H. Ohtake, S. Fukuda, B. Jinnai, T. Tatsumi, and S. Samukawa, *Jpn. J. Appl. Phys.* **49** (2010), 04DB14.